

1 **“Empirical pre-whitening” spectral analysis detects periodic but inconsistent signals in abyssal hill**
2 **morphology at the southern East Pacific Rise**

3

4 John A. Goff

5 *University of Texas Institute for Geophysics, Austin, Texas, USA*

6 goff@ig.utexas.edu

7

8 Submitted to *Geochemistry, Geophysics, Geosystems*, June, 2020

9

10

11

12 Key Points:

- 13 1. A new algorithm is formulated to detect periodicities embedded in an aperiodic process using
14 “empirical pre-whitening” spectral analysis
- 15 2. Periodicities are detected at the southern East Pacific Rise, but are spatially and temporally
16 inconsistent
- 17 3. The dominant aperiodic signal is likely fault-constructed, while ephemeral periodic signals may
18 relate to internal melt supply variations

19

20

21
22
23
24
25
26
27
28
29
30
31
32
33
34
35
36
37
38
39
40
41
42
43

Abstract. The existence, or not, of periodicities in abyssal hill morphology has been vigorously debated in recent publications, and some have hypothesized that such periodicities are evidence of the impact of Milankovitch cycle-caused sea level fluctuations on the volcanic construction process at mid-ocean ridges. Periodicities are detected by the presence of spectral peaks that rise significantly above the random variations of sample power spectra associated with an aperiodic, continuous spectrum process, typically modeled as a band-limited fractal (von Kármán model). Here I formulate and test a new algorithm to “empirically pre-whiten” the sample power spectrum which, without needing to model the continuous spectrum, flattens it to a zero-mean process. This greatly simplifies definition of the null hypothesis, and additional modeling approximates standard deviation levels that provide a conservative basis for detecting peaks that may be indicative of periodicity. The algorithm is applied to extensive bathymetric data flanking the southern East Pacific Rise. Significant periodicities are detected on many profiles analyzed, but the periods vary widely, and do not cluster at Milankovitch periods. The most substantial harmonic signals detected exhibit periods $\sim 0.082\text{-}0.216$ my, with root-mean square (RMS) heights approximately a quarter to a third of the RMS height for the aperiodic signal. It is hypothesized that the dominant aperiodic component of abyssal hills corresponds to morphology constructed by faults that follow a random distribution governed by scaling laws, whereas longer-scale periodic signals are associated with crustal thickness variations controlled internally by variations in melt supply.

Key Words: Mid-ocean ridge, faulting, melt supply, von Kármán model, stochastic processes, autocovariance

44 1. Introduction

45 A number of recent publications have endeavored to identify peaks in the sample power spectra
46 (periodograms) of abyssal hill bathymetry profiles, presumably indicative of periodicities that could be
47 interpreted as systemic temporal variations in mid-ocean ridge (MOR) processes (Crowley et al., 2015;
48 Tolstoy, 2015; Olive et al., 2016; Shinevar et al., 2019). Discovery of topographic periodicities would
49 greatly impact our understanding of variability in MOR processes, whether externally forced, such as
50 proposed Milankovitch Cycle dependence (Crowley et al., 2015; Tolstoy, 2015), or internally forced, such
51 as via modulations of mantle upwelling (Shinevar et al., 2019; Parnell-Turner et al., 2020). There are,
52 however, a number of potential pitfalls in these analyses, and it is quite possible that the spectral peaks
53 that have been discerned are instead typical random fluctuations of a sample power spectrum
54 estimated from an aperiodic time series, particularly if detection thresholds are not sufficiently
55 conservative.

56 As described in Priestley (1981), there are two end-member time series spectra: discrete and
57 continuous. Discrete spectra are those with one or more periodicities, detected by peaks on the sample
58 power spectrum at individual frequencies. Well-known methods are established for determining the
59 significance of those peaks as observed on a sample power spectrum in the presence of a background
60 white noise process. In contrast, continuous spectra processes are those that are characterized by a
61 smooth, continuous power spectral function $P(f)$ across a range of frequencies, f , and do not contain any
62 periodicities. However, sample power spectra derived from continuous-spectra time series are, in
63 Priestley's (1981) words, "erratic and wildly fluctuating", which is a result of two well-known properties:
64 (1) the variance of the sample power spectrum does not approach zero as the number of sample points
65 (N) approaches infinity, and (2) the correlation between two sample power spectrum points decreases
66 as N increases. Because of this erratic property, application of discrete-spectrum tests to continuous-
67 spectra processes "may indicate the existence of a large number of spurious periodic components",

68 according to Priestley (1981); the methods are not invalid, he states, but rather are misapplied when
69 used on time series with continuous spectra. Furthermore, since the variance of the sample power
70 spectrum scales with $P^2(f)$, such false detections are more likely where $P(f)$ is larger.

71 Between the discrete and continuous spectrum end members, Priestley (1981) describes a “mixed”
72 spectrum derived from the blending of time series of both periodic and aperiodic character, which is an
73 apt model for hypothesizing the existence of periodicities in abyssal hill morphology (Goff et al., 2018).
74 Abyssal hills are formed primarily by normal faults (McDonald et al., 1996; Durant et al., 1996;
75 Macdonald, 2015), whose throw and spacing can be modeled as random distributions that follow scaling
76 laws (Malinverno and Cowie, 1993; Bohnenstiehl and Carbotte, 2001). Abyssal hill morphology
77 statistical properties have been successfully characterized using a von Kármán functional form (von
78 Kármán, 1948), a continuous (aperiodic) spectrum that can also be described as a band-limited fractal
79 model (Goff and Jordan, 1988, Goff and Tucholke, 1997). Any periodic component of the seafloor
80 topography, such as might be caused by variations in crustal thickness, independent of the abyssal hill
81 faulting process, could be modeled as a superposition of periodic and aperiodic signals.

82 If we consider the aperiodic time series with continuous power spectrum, $P(f)$, to be a null
83 hypothesis, rejection of the null hypothesis would be established by observation of a spectral peak that
84 greatly exceeds the normal variation of the continuous sample power spectrum. However, to do this,
85 the null hypothesis must be defined, which requires either knowing $P(f)$ *a priori*, or modeling $P(f)$ by
86 fitting a functional form (e.g., Goff and Jordan, 1988). Vaughan (2005), for example, formulated a
87 methodology for detecting periodicities in the presence of a red (negative trend with frequency)
88 background noise, which can be fit with simple power-law, and where the null hypothesis variability
89 about this trend is characterized by a χ^2 distribution. Vaughan (2005) noted, however, that the
90 modeling fit itself adds additional uncertainty, leading him to strongly suggest that confidence levels 3-4
91 times the standard deviation (σ) should be applied when determining the significance of a spectral peak

92 in indicating a periodic component of a mixed spectrum, rather than the oft-assumed 2σ confidence
93 level.

94 Pre-whitening is another approach to assisting in the detection of periodicities in a mixed spectrum;
95 the general idea is to divide the sample power spectrum by $P(f)$ so that the overall trend is flat; i.e., it
96 emulates a discrete spectrum in the presence of white noise. In this construction, standard tests for the
97 significance of observed peaks can be applied (Priestley, 1981). The spectral analysis methodology
98 employed by Crowley et al. (2015) and emulated by others (Olive et al., 2016; Shinevar et al., 2019),
99 does indeed attempt to apply pre-whitening to the spectrum. However, no attempt was made in these
100 analyses to estimate $P(f)$, applying instead simple f^2 multiplicative factor that fails to flatten the
101 spectrum. Rather, because abyssal hills are band-limited in their power-law (i.e., fractal) behavior, this
102 attempt at pre-whitening causes the spectrum to arc, artificially enhancing positive spectral fluctuations
103 near the apex of the arc to appear more significant than they likely are. Although modeling the
104 spectrum using the von Kármán function would undoubtedly improve pre-whitening, Priestley (1981)
105 argues against pre-whitening in this way because, if there is indeed a periodic component, it will distort
106 the modeling of $P(f)$ in a way that adversely affects both that estimation and the ultimate detection of
107 periodic signals.

108 Harmonic components of a mixed spectrum profile can also be detected using multitaper techniques
109 (Thomson, 1990; Percival and Walden, 1993; Mann and Lees, 1996; Crowley et al., 2015). Multitaper
110 spectral estimation applies an orthogonal series of tapers to a time series, Fourier transforms each and
111 then adds the results together to form a sample power spectrum. This technique is widely used to
112 reduce the variability of the power spectrum estimate in comparison to the periodogram, and eliminate
113 spectral leakage (e.g., McCoy et al., 1998; Babadi and Brown, 2014). An embedded harmonic signal may
114 be detected by an F-test for phase-coherent variability at any one frequency across taper components
115 (Thomson, 1990; Mann and Lees, 1996). However, phase coherence does not necessarily imply

116 significance with respect to the variability associated with the aperiodic component of the process at
117 that frequency (Mann and Lees, 1996). Alternatively, or in addition to the F-test, the height of a spectral
118 peak can be compared against an assumed χ^2 distribution on local variability about the null hypothesis,
119 which is represented by the best estimate of $P(f)$ for the multitaper estimate of the power spectrum
120 (Percival and Walden, 1993; Mann and Lees, 1996; Crowley et al., 2015). This test is akin to the
121 procedure Vaughan (2005) utilized for the periodogram.

122 To obviate the need to model $P(f)$ for defining the null hypothesis and/or for pre-whitening,
123 Priestley (1981; Chapter 8) proposed an ingenious and simple solution that he termed the “ $P(\lambda)$ ” test.
124 The method utilizes the sample autocovariance function, which is the Fourier transform pair of the
125 sample power spectrum. The sample autocovariance consists of two components: (1) a central,
126 decaying portion that includes all information about the functional nature of the continuous, aperiodic
127 spectrum $P(f)$, and (2) a long tail that randomly fluctuates about 0 and, should they be present, also
128 includes harmonic fluctuations associated with periodic components of the time series because they do
129 not decay to zero with increasing lag. Priestley’s (1981) method consists of zeroing-out the central,
130 decaying portion of the sample autocovariance (which can be determined by simple inspection rather
131 than modeling), and then Fourier-transforming the remaining tails; the result will be a zero-mean (null
132 hypothesis), randomly fluctuating function, with positive spikes at frequencies if and where periodic
133 signals are present (deviation from null hypothesis). Despite the relative simplicity and elegance of the
134 $P(\lambda)$ test, a literature search found very few examples of its application (e.g., Bhansali, 1977; Garrido and
135 Garcia, 1992). For clarity in terminology, I propose the term “empirical pre-whitening” to describe this
136 simple technique.

137 In this paper I present a new algorithm for utilizing Priestley’s (1981) “ $P(\lambda)$ ”/empirical pre-whitening
138 method to detect periodic signals in a mixed-spectra process. I first test the algorithm on synthetic
139 profiles generated by adding cosine functions of various amplitude and frequency to an aperiodic time

140 series corresponding to the von Kármán statistical model (Goff and Jordan, 1988). The algorithm is able
 141 to accurately detect the periodic components provided the amplitude is sufficient to rise significantly
 142 above the random fluctuations associated with the aperiodic component of the spectrum at that
 143 frequency. I then apply this algorithm to twelve bathymetric profiles of abyssal hill morphology along
 144 the southern East Pacific Rise (EPR) to test for the presence of periodicities. A portion of this region was
 145 also used by Tolstoy (2015) in a spectral analysis that discerned a ~100 ky periodicity, which is one of the
 146 Milankovitch periods. The profiles are converted from distance to crustal age versus depth using an
 147 existing, high-resolution age model for the region (Goff et al., 2018).

148

149 **2. Formulation**

150 The following formulation is based on Priestley (1981; Section 8.4). Consider a discrete time or space
 151 series X_i , $1 \leq i \leq N$, evenly space by ΔX . Consider further that X_i represents the summation of two
 152 independent, zero-mean, stationary processes Y_i and Z_i , where Y_i is an aperiodic process with a
 153 continuous spectrum, and Z_i is represented by one or more sinusoidal forms. The autocovariance of X_i ,
 154 $R_X(s)$, is then represented by:

$$155 \quad E[X_i X_{i+s}] = R_X(s) = R_Y(s) + R_Z(s), \quad (1)$$

156 where $E[\cdot]$ is the expectation operator, s is the lag index, and $R_Y(s)$ and $R_Z(s)$ are the autocovariances of Y_i
 157 and Z_i , respectively. Because Y_i is aperiodic, $R_Y(s)$ will decay monotonically with increasing $|s|$. Because
 158 Z_i has periodic elements, $R_Z(s)$ will also vary sinusoidally for all s ; each sinusoidal element, defined by a
 159 frequency f amplitude and amplitude α , will contribute a term $\frac{1}{2} \alpha^2 \cos(2\pi s f)$ to $R_Z(s)$. The sample
 160 autocovariance, i.e., estimation of $R_X(s)$ based on samples X_i , is given by:

$$161 \quad \hat{R}_X(s) = \frac{1}{N-s} \sum_{i=1}^{N-s} X_i X_{i+s}, \quad 0 \leq s \leq N/2$$

$$162 \quad \hat{R}_X(-s) = \hat{R}_X(s). \quad (2)$$

163 The power spectrum of X_i , denoted by $P_X(f)$, is the Fourier transform conjugate of $R_X(s)$, and we can
 164 likewise define the power spectra of Y_i and Z_i in the same way such that

$$165 \quad P_X(f) = P_Y(f) + P_Z(f). \quad (3)$$

166 The sample power spectrum can be computed in two equivalent ways:

$$167 \quad \hat{P}_X(f) = DFT[\hat{R}_X(s)], \text{ or} \quad (4)$$

$$168 \quad \hat{P}_X(f) = |DFT[X_i]|^2, \quad (5)$$

169 where DFT indicates the discrete Fourier transformation. Equation (5) is far more commonly utilized since
 170 it does not require the extra step of computing the sample autocovariance as in Equation (2). However,
 171 Equation (4) is utilized here because it provides a mechanism for separating periodic from aperiodic
 172 components of the spectrum. Priestley (1981) proposes in his “ $P(\lambda)$ ” test to first inspect $\hat{R}_X(s)$ after
 173 computing it in order to identify a value m such

$$174 \quad R_Y(s) \sim 0, |s| \geq m. \quad (6)$$

175 In other words, we seek to identify that portion of the sample autocovariance which is monotonically
 176 decaying, and which contains all the structural information that constrains the continuous portion of the
 177 power spectrum $P_Y(f)$. The remainder, or “tail,” is a zero-mean signal that, if there are no periodic
 178 elements in X_i , will fluctuate randomly (and which, after DFT, contributes to the erratic fluctuations of
 179 $\hat{P}_X(f)$). If, however, there are periodic elements, then those will be present in the tail, as noted above.

180 The next step in Priestley’s (1981) method is thus to remove the monotonically decaying portion of
 181 $\hat{R}_X(s)$ by zeroing it out for $|s| < m$:

$$182 \quad \hat{R}_X^m(s) = \begin{cases} 0, & |s| < m \\ \hat{R}_X(s), & |s| \geq m \end{cases}. \quad (7)$$

183 Finally, this altered sample autocovariance is transformed to create the “empirically pre-whitened”
 184 spectrum

$$185 \quad \hat{P}_X^m(f) = DFT[\hat{R}_X^m(s)]. \quad (8)$$

186 In practice, the “cut” edges at $|\pm s| = m$, as well as the ends of the function at $|\pm s| = N/2$, need to be
187 tapered prior to the DFT in order to minimize spectral leakage.

188 In the case of the null hypothesis, where no periodicity is present and $P_X(f) = P_Y(f)$, Priestly (1981)
189 demonstrates that

$$190 \quad E[\hat{P}_X^m(f)] = 0, \quad (9)$$

191 and

$$192 \quad VAR[\hat{P}_X^m(f)] \sim \frac{N-2m}{2} P_Y^2(f), \quad (10)$$

193 where VAR indicates the variance. Therefore, the standard deviation on the null hypothesis, σ , is
194 estimated by the square root of Equation (10). Deviation from the null hypothesis can be established by
195 observation of spectral peaks that significantly deviate from the typical erratic variability associated with
196 the continuous component of the spectrum. For this purpose, a conservative criterion must be applied.
197 Depending on N , the empirically pre-whitened spectrum could have hundreds or thousands of peaks
198 and valleys, so that numerous peaks are expected to surpass a 2σ (95%) threshold, and even several are
199 likely to surpass a 3σ (99%) threshold without the presence of a periodic signal. In the following
200 analyses, a value of 3.5σ will be used as a minimum detection threshold.

201 Equation (10) does require knowledge of the underlying continuous spectrum $P_Y(f)$. Where $P_Y(f)$ is
202 not known *a priori*, it must be modeled by fitting a smooth functional form to the sample
203 autocovariance or sample power spectrum. This will be demonstrated in Section 4. Addition of periodic
204 components will increase the overall variance of the profile compared to the null hypothesis, thus
205 increasing the modeled value of $P_Y(f)$ and subsequent estimation of σ . Fortunately, this has the effect of
206 increasing the confidence in detection of periodic contributions, since the level of significance of a
207 spectral peak should be considered a minimum value.

208

209 **3. Synthetic Test**

210 To test the ability of an empirically pre-whitened spectrum to detect periodic elements of a mixed
 211 spectrum process, I constructed a series of synthetic profiles consisting of the addition of an aperiodic
 212 time series, generated from the von Kármán statistical model, and cosine functions of varying amplitude
 213 and frequency. The von Kármán statistical model can be expressed equivalently in either
 214 autocovariance or power spectral form (Goff and Jordan, 1988; Goff and Tucholke, 1997). For the
 215 autocovariance:

$$216 \quad R_{VK}(s) = H^2 G_\nu[k_0 s] / G_\nu(0) \quad (11)$$

217 where H is the RMS height, k_0 is a scaling parameter with dimensions time^{-1} (or distance^{-1}), and G_ν is
 218 defined by

$$219 \quad G_\nu(x) = x^\nu K_\nu(x). \quad 0 \leq x < \infty. \quad (12)$$

220 K_ν is the modified Bessel function of the second kind and order ν . At $\nu = 1/2$, $R_{VK}(s)$ is an exponential
 221 function. The functional form of the von Kármán power spectrum for a profile is given by:

$$222 \quad P_{VK}(f) = \frac{\Gamma\left(\nu + \frac{1}{2}\right)}{\Gamma(\nu)} \frac{2H^2 \sqrt{\pi} (k_0/2\pi)^{2\nu}}{((k_0/2\pi)^2 + f^2)^{\nu + \frac{1}{2}}} \quad (13)$$

223 where Γ is the gamma function. In the power spectral formulation, $k_0/2\pi$ serves as a corner frequency:
 224 for $f \gg k_0/2\pi$, $P_{VK}(f)$ is a power-law form (i.e., red spectrum, or fractal), while for $f \ll k_0/2\pi$, $P_{VK}(f)$ is a
 225 constant (i.e., white spectrum). The order parameter ν determines the Hausdorff, or fractal dimension:

$$229 \quad D = E + 1 - \nu, \quad (14)$$

230 where E is the Euclidian dimension (i.e., $E = 1$ for a profile).

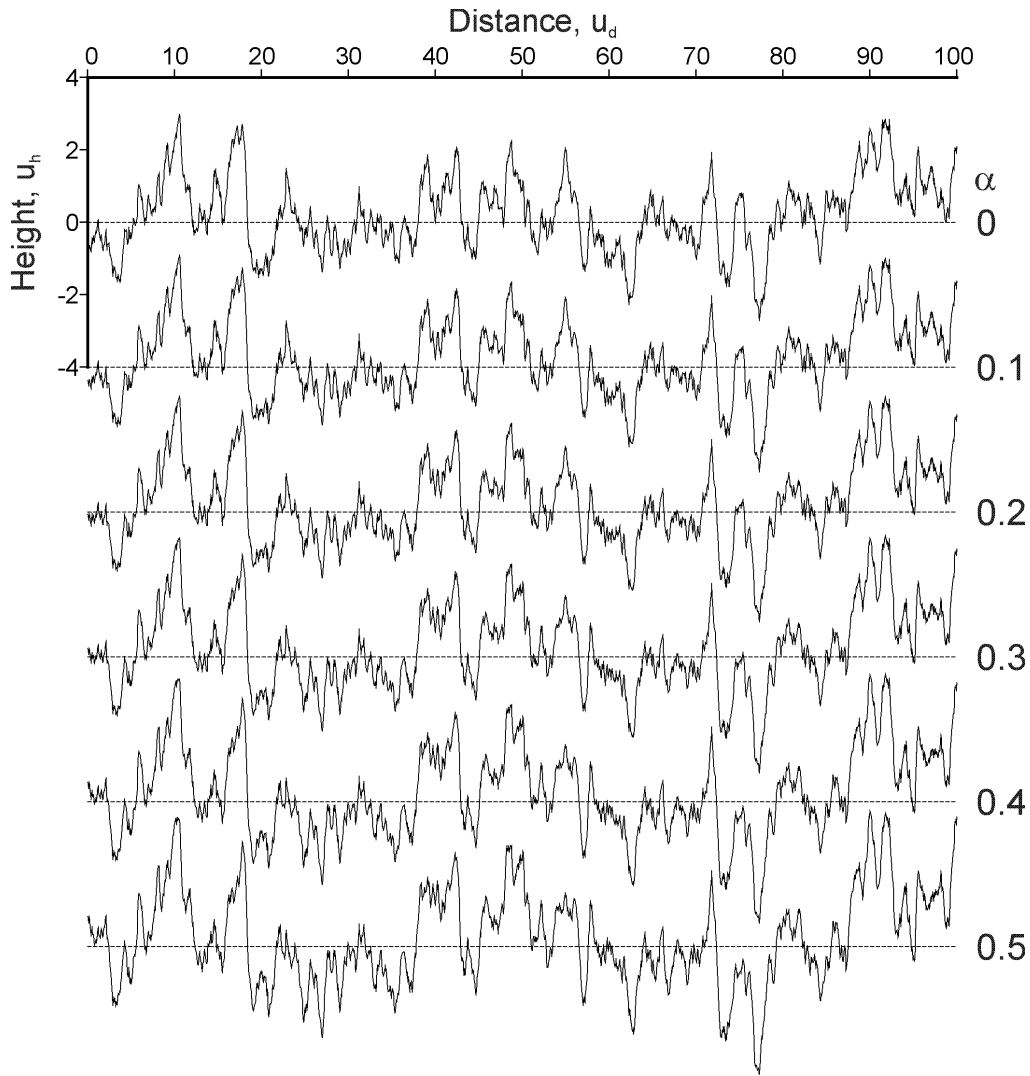
231 A synthetic profile conforming to the von Kármán statistical model can be generated by: (1)
 232 multiplying the amplitude spectrum (square root of Equation (13)) by a random phase $\exp(i\phi)$, where ϕ
 233 is a uniform random value distributed on $(0, 2\pi]$, (2) enforcing Hermetian symmetry over negative

234 frequencies, and (3) transforming to the space domain by DFT (Goff and Jordan, 1988; Goff, 1995). The
235 uniform random phase results in a Gaussian distribution of profile values. In practice, a larger profile
236 than required should be generated, and then cropped to size in order to fully randomize the sample
237 power spectrum of the synthetic profile.

238 For the synthetic experiment, parameters chosen were: $H = 1 u_h$, $k_0 = 1 u_d^{-1}$, and $\nu = 0.8$, where u_h
239 and u_d are arbitrary units of height and distance (or time), respectively. The profile length is 10,000
240 points with a node spacing of $\Delta X = 0.05 u_d$. The top profile of Figure 1 displays the profile generated
241 with these parameters. To generate a mixed-spectrum profile, $X_M(i\Delta X)$, I superpose cosine functions on
242 the von Kármán profile using:

$$243 \quad X_M(i\Delta X) = X_{VK}(i\Delta X) + \alpha[\cos(i\Delta X 2\pi f_1) + \cos(i\Delta X 2\pi f_2) + \cos(i\Delta X 2\pi f_3)], \quad (15)$$

244 where $X_{VK}(i\Delta X)$ is the profile generated with the von Kármán statistical model, and f_1, f_2 and f_3 are
245 frequencies chosen to be 0.02, 0.1, and 0.5 cycles/ u_d , respectively. Figure 1 displays the results of
246 Equation (15) for values of α ranging from 0 to 0.5. A surprising observation regarding these profiles is
247 that they look very similar; i.e., that the harmonic components are not visually self-evident, even at the
248 largest value of α . This observation can be understood by considering the contribution of each
249 sinusoidal component to the overall RMS height. For example, at $\alpha = 0.3 u_h$, the variance is of the
250 sinusoidal component is $\frac{1}{2}\alpha^2$, or $0.045 u_h^2$. Added to the aperiodic variance of $1 u_h^2$, the combined
251 variance is $1.045 u_h^2$, and taking the square root yields an overall RMS of $1.022 u_h$. Thus, the addition of
252 one sinusoidal component of amplitude $0.3 u_h$ increases the RMS by only 2.2%.



253

254 Figure 1. Synthetic profiles constructed using Equation (15) and parameters listed in the text. The
 255 vertical scale corresponds to the $\alpha = 0$ profile; all others are offset a constant distance for visualization.
 256 The first 100 u_d of each synthetic profile, out of a total distance of 500 u_d , are plotted.

257

258 In contrast to the profiles, the sample autocovariances of these profiles (Figure 2) display clear visual

259 evidence of the harmonic components, which come to dominate the tails as α increases because they do

260 not decorrelate as lag increases, as the aperiodic signal does. This is a clear visual confirmation of the

261 utility of the sample autocovariance to isolate the harmonic components of a mixed spectrum process

262 from the aperiodic components. Using these sample autocovariances, I have conducted a spectral

263 analysis where I compare (1) the sample power spectrum computed by DFT of the full sample

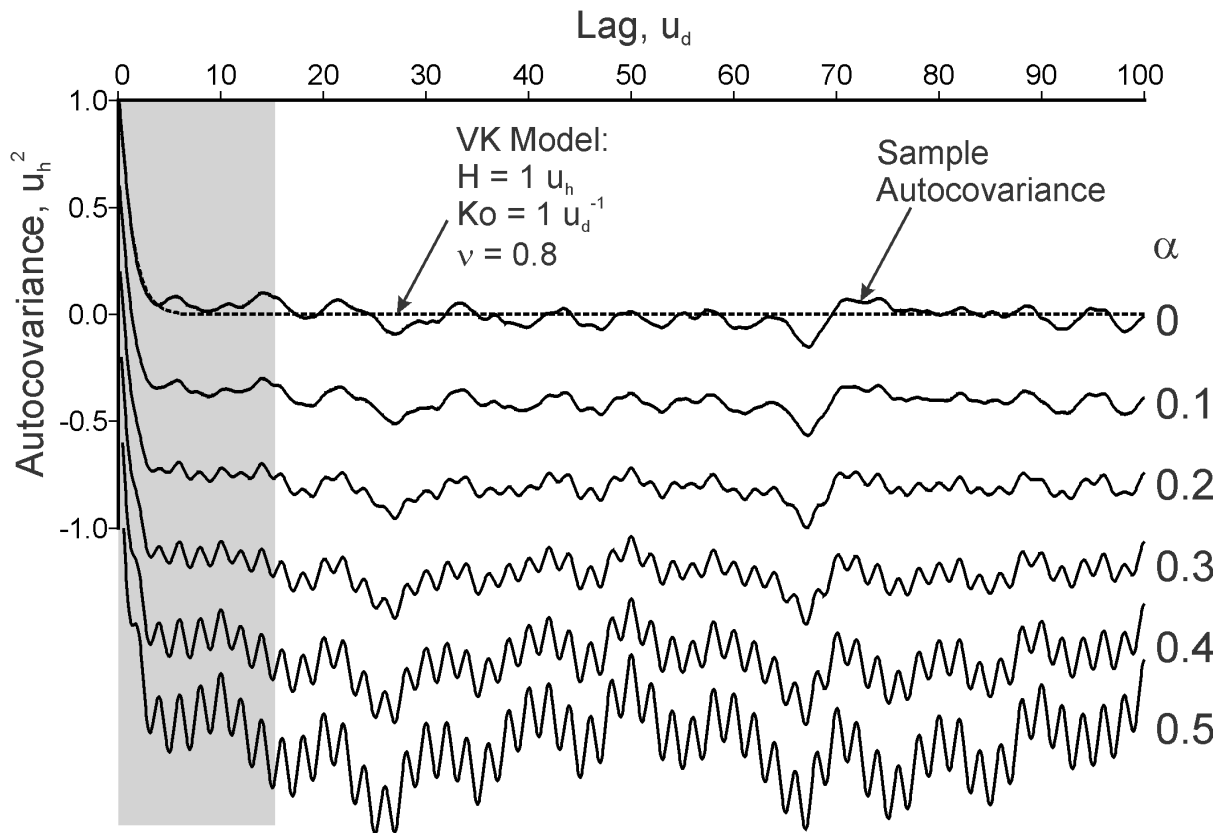
264 autocovariance, and (2) the empirically pre-whitened spectrum computed by DFT of the sample

265 autocovariance after zeroing-out the shaded regions shown in Figure 2, which self-evidently includes the
266 full span of the monotonically-decaying portion of the function. In addition, a \cos^2 taper is applied over
267 10% of the profile at each edge to suppress spectral leakage. The full suite of results is presented in the
268 Supplementary Material, and cases $\alpha = 0 u_h$ and $\alpha = 0.3 u_h$ are presented in Figures 3 and 4, respectively,
269 to illustrate key findings.

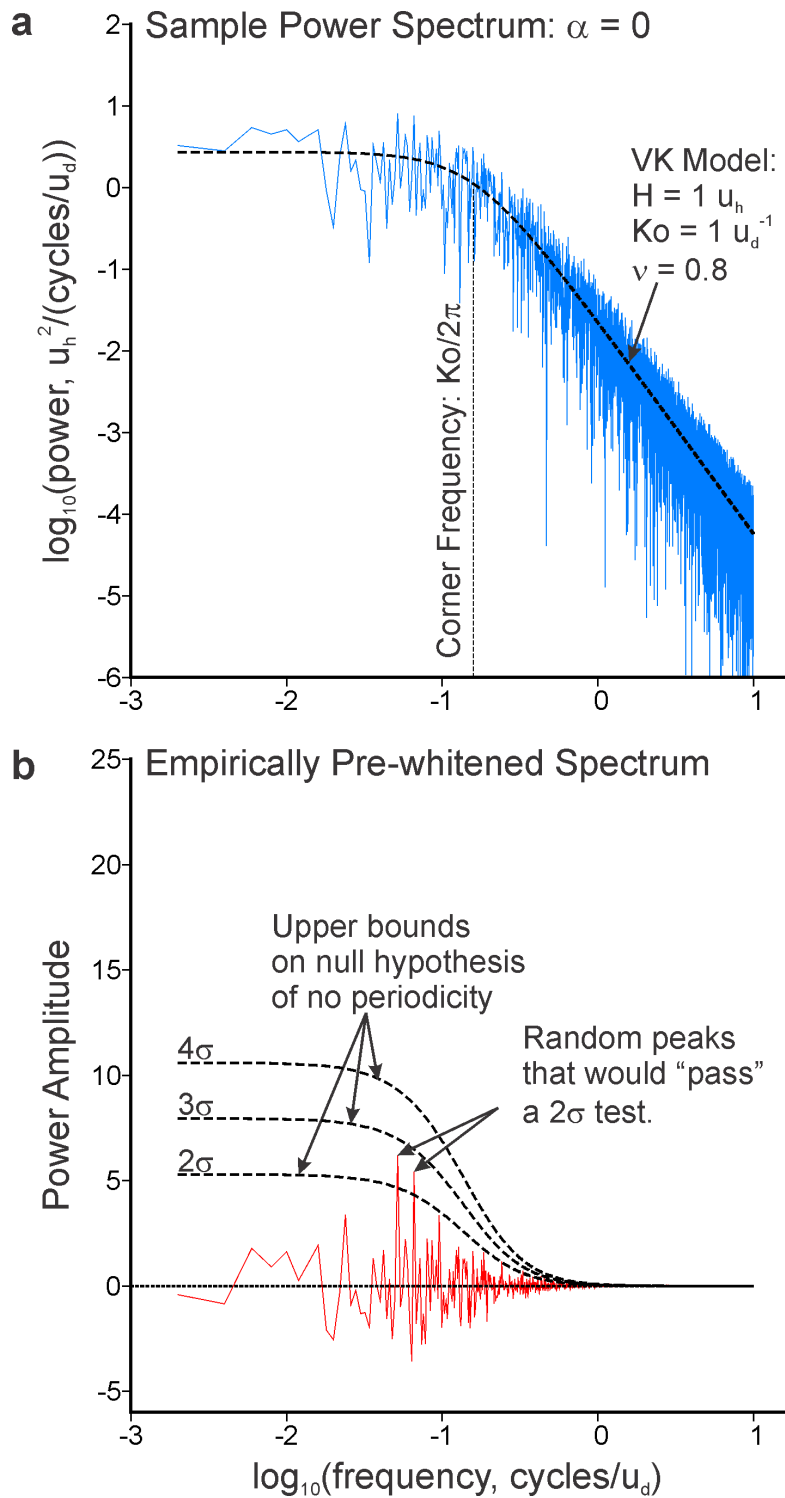
270 The null ($\alpha = 0 u_h$) case is presented in Figure 3. As noted earlier, the von Kármán statistical model is
271 a band-limited fractal, following a power-law form (negative linear trend on a log-log plot) at high
272 frequencies, and flat at low frequencies, with the transition governed by the corner frequency. The
273 sample power spectrum from the synthetic profile (Figure 3a) closely follows this functional form, as
274 expected, but with the highly erratic variability that is characteristic of continuous-spectrum, aperiodic
275 profile. The empirically pre-whitened spectrum for the null case (Figure 3b), is also highly erratic, but
276 with a mean of zero which indicates success in removing the structural form of the continuous power
277 spectrum. Comparison between Figures 3a and 3b demonstrates that the variations of the sample
278 power spectrum about the model function are retained in the variation of the empirically pre-whitened
279 spectrum about zero. The 2σ upper bound does well in characterizing the envelope of variability, which
280 increases as f decreases, but is not a hard limit; at least two peaks are observed to exceed 2σ , which is
281 expected statistically.

282 The $\alpha = 0.3 u_h$ case is presented in Figure 4. Frequency f_3 (0.5 cycles/ u_d) is detectable at $\alpha = 0.1 u_h$
283 (Supplementary Material) owing to the fact that the variations of the aperiodic component of the profile
284 are very small at this frequency. Frequencies f_1 (0.02 cycles/ u_d) and f_2 (0.1 cycles/ u_d), however, are only
285 detectable at $>3.5\sigma$ for $\alpha = 0.3 u_h$ (Figure 4b) and larger (Supplementary Material). Because they all
286 have the same amplitude, the peaks at all three frequencies are expected to be of the same height on
287 the empirically pre-whitened spectrum. However, the peak at f_2 is observed to be less than the peaks at
288 f_1 and f_3 by about 25% (Figure 4b). This emphasizes an important point: the height of the discrete

289 spectral peaks are modulated by the random highs and lows of the continuous spectrum upon which it is
 290 superposed, leading to uncertainty in detection and measurement of amplitude (which will be
 291 considered in the next section).

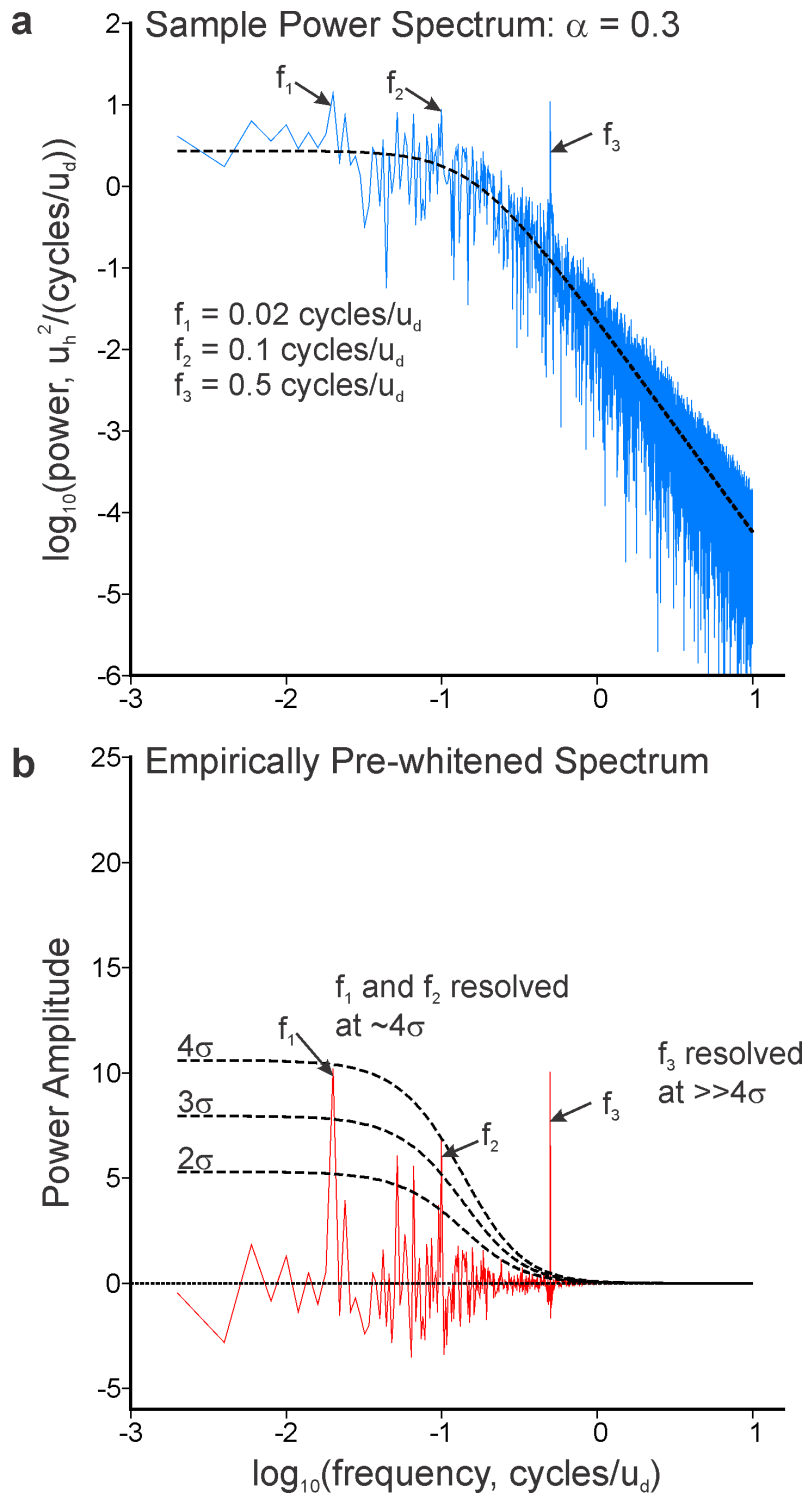


292
 293 Figure 2. Sample autocovariance functions (solid) computed from profiles shown in Figure 1, plotted to a
 294 lag of $100 u_d$. The von Kármán (VK) statistical model autocovariance, from which the synthetic profiles
 295 were generated, is overlain (dashed). The vertical scale corresponds to the $\alpha = 0$ function; all others are
 296 offset a constant distance for visualization. For Figures 3 and 4, the discrete Fourier transformation of
 297 the sample autocovariance (with Hermetian symmetry) is used to compute the sample spectral density,
 298 while the empirically pre-whitened spectrum is computed in the same way after values in the shaded
 299 region are zeroed out. The number of values zeroed out is determined by inspection, ensuring that the
 300 full span of the decaying portion of the autocovariance is removed and leaving only a fluctuating, zero-
 301 mean tail. A value of $\alpha = 0$ is the null condition of no periodic component to the sample profile. Periodic
 302 components come to dominate the tail of the autocovariance with increasing α , compared to the far
 303 more subtle visual impact evidenced in the synthetic profiles of Figure 1.



304

305 Figure 3. (a) Sample power spectrum and (b) empirically pre-whitened spectrum calculated from the $\alpha =$
 306 0 sample autocovariance shown in Figure 2. The von Kármán model is overlain on the power spectral
 307 density, and the 2σ , 3σ , and 4σ upper bounds on the null hypothesis are overlain on the empirically pre-
 308 whitened spectrum. Examples of "false positive" detection of periodic components are observed in the
 309 if the 2σ bound is used as a threshold.



310

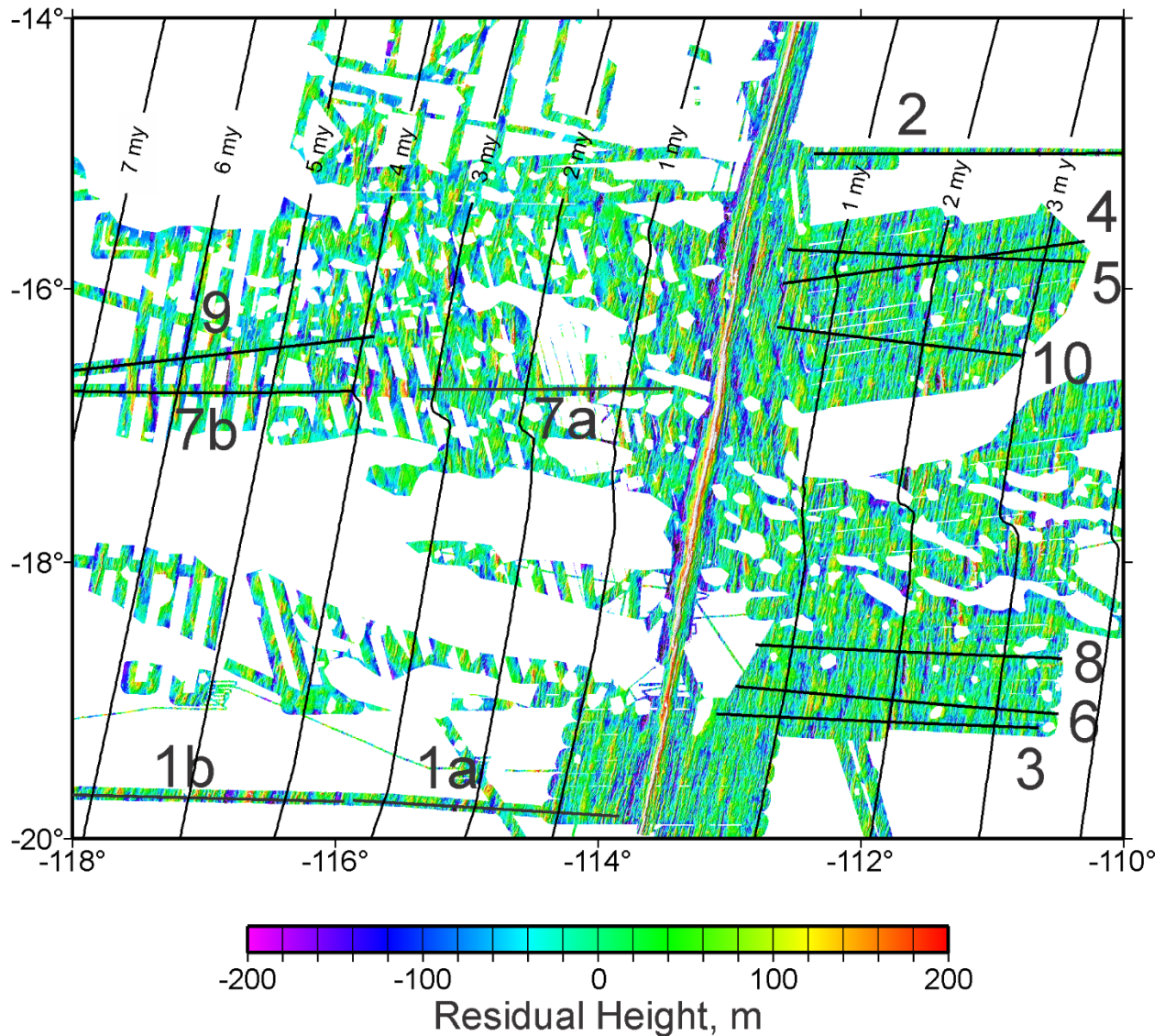
311 Figure 4. (a) Sample power spectrum and (b) empirically pre-whitened spectrum calculated from the $\alpha =$
 312 0.3 sample autocovariance shown in Figure 2. The von Kármán model is overlain on the power spectral
 313 density, and the 2σ , 3σ , and 4σ upper bounds on the null hypothesis are overlain on the empirically pre-
 314 whitened spectrum. All three harmonic components are resolved at $> 3.5\sigma$ in this example.
 315

316 This synthetic experiment demonstrates the efficacy of the empirically pre-whitened spectrum in
317 detecting periodic components of a mixed spectrum profile. Even with a conservative detection
318 criterion of 3.5σ , positive identification was made of harmonic signals that add only 2.2% each to the
319 overall RMS variability. The certainty of detection increases as the amplitude of the sinusoidal
320 component increases (Supplementary Material), providing confidence that any substantial harmonic
321 component to the profile will be detected. The empirical pre-whitening algorithm has the potential for a
322 wide variety of applications.

323

324 **4. Application to the Southern East Pacific Rise**

325 The southern East Pacific Rise (Figure 5) is the site of some of the most extensive publically-available
326 multibeam bathymetric coverage in the world of a mid-ocean ridge (MOR) and its flanks (Scheirer et al.
327 1996). The region also exhibits some of the fastest MOR spreading rates (~ 7.7 - 7.8 cm/yr half rates
328 DeMets et al., 1990). Tolstoy (2015) applied a spectral analysis in a limited area of this region and found
329 a spectral peak at a period of ~ 100 ky, inferring that Milankovitch cycles may be influencing volcanic
330 construction at the MOR. Goff et al (2018) further fine-tuned the Müller et al. (2016) age model for this
331 region, and applied a stacking analysis to identify any temporal variations in bathymetry that were
332 coherent across the region, which would be expected if the rise and fall of sea-level associated with
333 Milankovitch cycles, and external forcing, were controlling abyssal hill construction. They found,
334 however, that there was no evidence for spatially coherent temporal signals, periodic or otherwise.
335 Nevertheless, lack of synchronicity does not imply lack of periodicity. Rather than an external forcing
336 that affects the MOR uniformly either globally or regionally, variations in volcanic output might be
337 internally forced within the mantle (Shinevar et al., 2019; Parnell-Turner et al., 2020), which could be
338 periodic (or at least episodic) and which may vary in period, phase and amplitude from one segment to
339 the next. If so, then the stacking analysis of Goff et al. (2018) would not detect such signals.



341

342 Figure 5. Multibeam bathymetry along the flanks of the southern East Pacific Rise, high-pass filtered
 343 with a 40 km box filter and masked to removed seamounts (modified from Goff et al., 2018). Crustal
 344 ages are contoured at 1 my increments (Muller et al., 2016; Goff et al., 2018). Profiles used for analysis
 345 are indicated by thick black lines and numbered identifiers.

346

347 To search for possible temporal periodicities, I have selected 12 profiles of residual height (Figure 5)
 348 and converted to age versus residual height using the crustal age model presented in Goff et al. (2018).
 349 Each profile is ~2.5-3 my long, resampled at a uniform interval of 0.0025 my, and linearly interpolated
 350 over any gaps in coverage. Such gaps were few as profiles were carefully selected to correspond to

351 swaths of nearly complete coverage and no seamounts. Profiles were also restricted to ages > 0.5 my to
352 avoid the MOR axial high and associated negative sidelobes that form with the high-pass filter of the
353 original bathymetry.

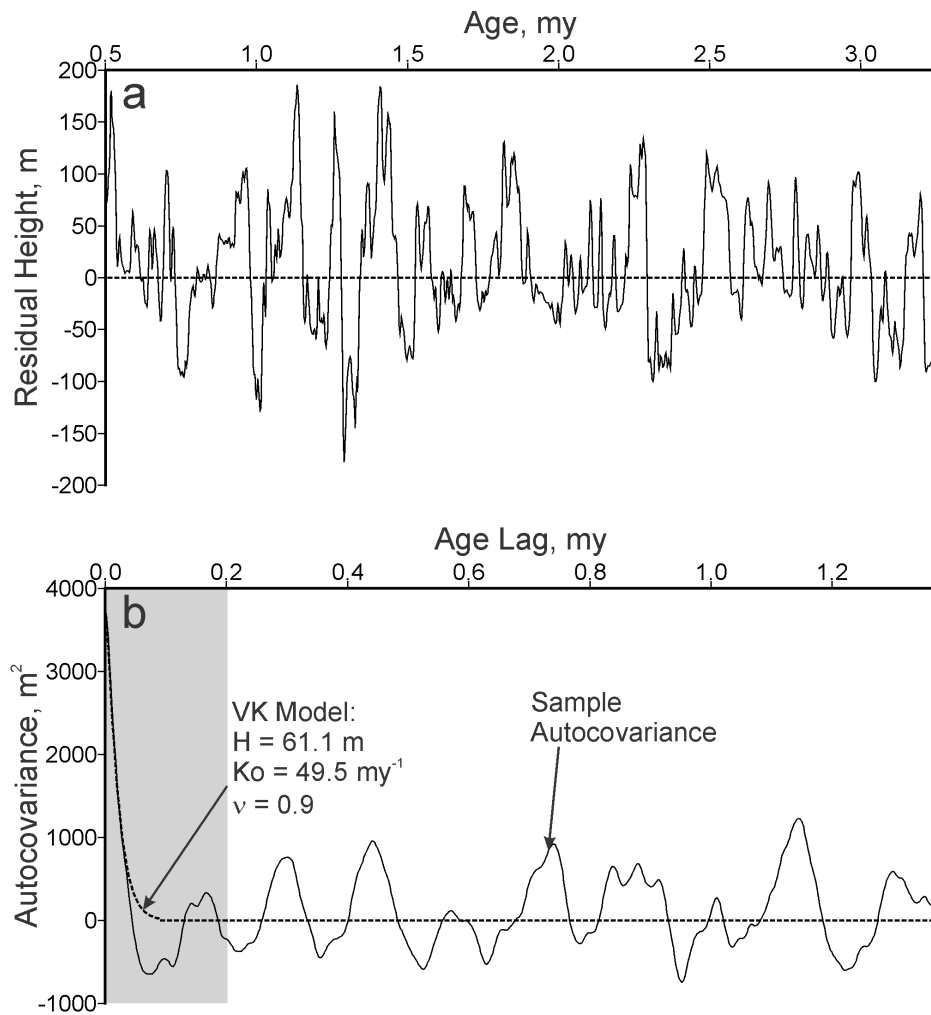
354 For example purposes, I present here the full analysis of Profile 7a (Figures 6 and 7), which is one of
355 the more convincing detections of a periodic component. The full suite of profiles analyses are
356 presented in the Supplementary Material, with results listed in Table 1. The age-versus-residual height
357 values for Profile 7a are shown in Figure 6a, and its sample autocovariance function is shown in Figure
358 6b. A von Kármán model is fit to the sample autocovariance (Figure 6b) via weighted, least-squares
359 inversion as formulated in Goff and Jordan (1988). The estimated value for RMS height, H , is 61.1 ± 4.7
360 m, and the scale parameter, k_0 , is $68.3 \pm 13.8 \text{ my}^{-1}$. Estimation of the parameter ν tends to become
361 unstable as it approaches its upper limit of 1 (Goff, 1991); that was the case here and in most of the
362 estimations in this analysis, and was assumed to be 0.9. A characteristic time, λ_0 , can be defined by the
363 width, or second moment of the autocovariance model (Goff and Jordan, 1988):

$$364 \quad \lambda_0 = \frac{\sqrt{2(\nu+1/2)}}{k_0}. \quad (16)$$

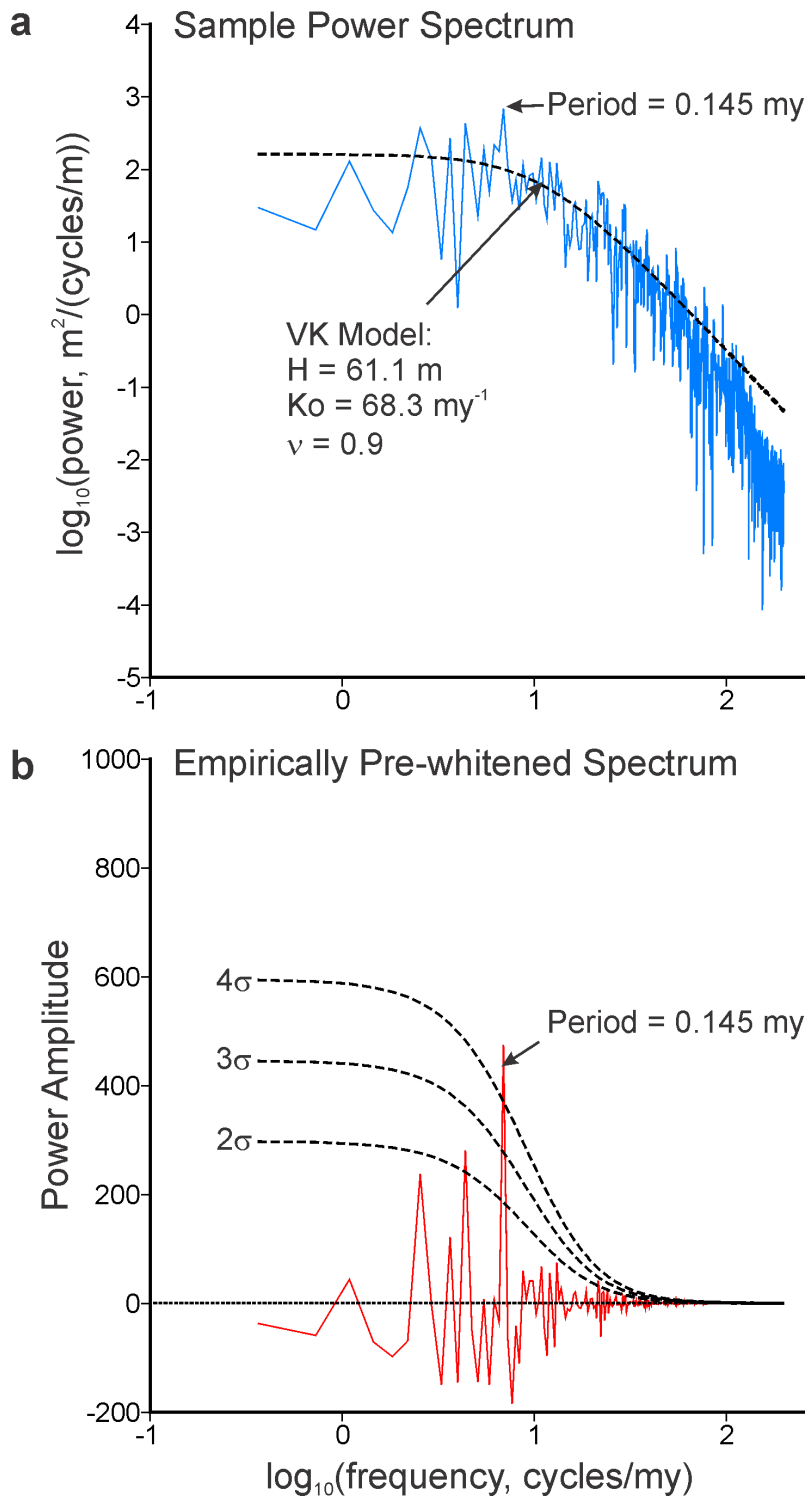
365 The characteristic time roughly corresponds to the visually dominant (on average) peak-to-peak distance
366 (Goff, 1991), and thus is an important point of comparison for any potential identification of a harmonic
367 component. For Profile 7a, $\lambda_0 = 0.049 \pm 0.010 \text{ my}$ (which equates to $\sim 3.8 \text{ km}$). The tail of the sample
368 autocovariance (Figure 6b) exhibits a number of evidently regularly-space peaks and troughs that
369 strongly suggest the presence of a harmonic component to the profile.

370 The spectral analysis of Profile 7a is shown in Figure 7. The sample power spectrum (Figure 7a)
371 follows the modeled von Kármán power spectrum well at lower frequencies, but deviates at the higher
372 frequencies. This deviation from the power law trend is a phenomenon noted by Goff and Jordan
373 (1988), who attributed it to the “response”, or beam width of the multibeam echosounder being larger
374 than the sample interval. This effect may also be caused by the averaging associated with the gridding

375 process. In any case, it is not a concern in this analysis because any periodic elements at that scale
 376 would exhibit very small amplitudes. In addition to the overall von Kármán-like trend, a noticeable peak
 377 is observed corresponding to a period of 0.145 my, approximately three times the characteristic time of
 378 the best-fitting von Kármán model. That same peak is shown on the empirically pre-whitened spectrum
 379 (Figure 7b) to be significant at a very high level of confidence: 5.1σ . Therefore, it can be stated that a
 380 periodic signal, with period of 0.145 my, is present in Profile 7a with a very high degree of certainty.



381
 382 Figure 6. (a) Bathymetric profile 7a converted from distance to age on the x-axis using the age model of
 383 Goff et al. (2018); location shown in Figure 5. (b) Sample autocovariance (solid) computed from (a), with
 384 best-fit von Kármán model (dashed). The power spectral density in Figure 7a is computed by discrete
 385 Fourier transform of the full sample autocovariance (with Hermetian symmetry), whereas the
 386 empirically pre-whitened spectrum in Figure 7b is computed in the same way after zeroing out the
 387 shaded region that fully encompasses the structural (non-zero mean) portion of the autocovariance and
 388 tapering the edges.



389

390 Figure 7. (a) Sample power spectrum and (b) empirically pre-whitened spectrum calculated from the
 391 sample autocovariance of Profile 7a shown in Figure 6b. The best-fit von Kármán model is overlain on
 392 the power spectral density, and the 2σ , 3σ , and 4σ upper bounds on the null hypothesis are overlain on
 393 the empirically pre-whitened spectrum. One harmonic component at a period of 0.145 my is detected
 394 at 5.1σ confidence

395 Having identified a likely periodic signal, the next step is to estimate its amplitude, α . That value can
396 be estimated from the amplitude of the peak observed on the empirically pre-whitened spectrum,
397 which is proportional to α^2 (Priestley, 1981). However, the coefficient is a complex function of N , m and
398 the tapers used prior to DFT of $\hat{P}_X^m(f)$. Priestly (1981) calculated closed-form approximations for linear
399 or no tapers, neither of which I found appropriate to the application at hand. Rather than attempt the
400 same calculation for the \cos^2 tapers used here, a far simpler method is to generate a simple cosine
401 function and pass it through the same spectral analysis applied to the data profile. Then, α is adjusted
402 until the height of the resulting spectral peak matches what is observed on the empirically pre-whitened
403 spectrum. With this procedure I estimated α to be ~ 30 m for the 0.145 my period peak detected for
404 Profile 7b. The variance of this sinusoidal contribution is $\alpha^2/2 = 450 \text{ m}^2$, which equates to an RMS of 21.2
405 m. The overall variance of Profile 7a is $H^2 = 3730 \text{ m}^2$. Therefore, $3730 \text{ m}^2 - 450 \text{ m}^2$, or 3280 m^2 of the
406 total variance of Profile 7a, is attributed to the aperiodic component of the profile. This equates to an
407 RMS of 57.3 m, and which is 2.7 times the RMS of the sinusoidal component. Thus, while significant in
408 its measurability, the sinusoidal contribution at 0.145 my period represents a relatively minor
409 component of Profile 7a compared to the aperiodic signal.

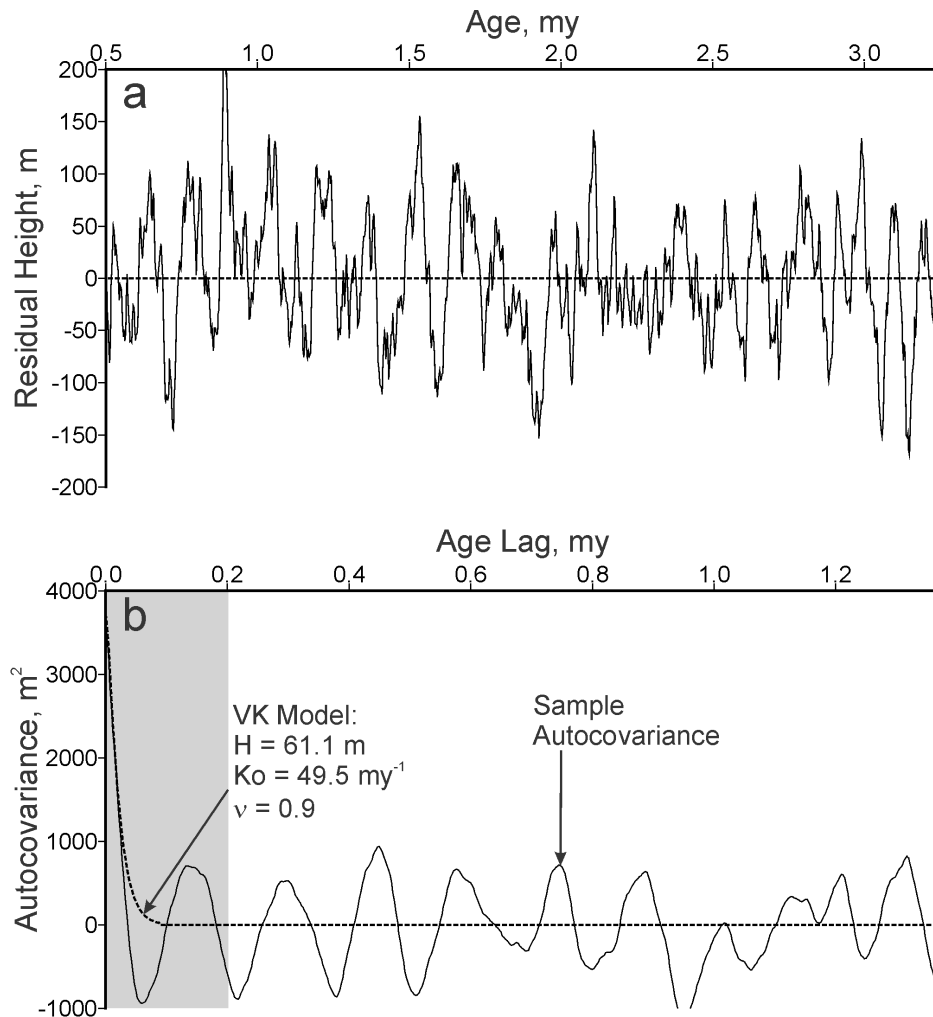
410 I next test the ability of the mixed spectrum statistical model, of the form presented in Equation
411 (15), to match these observations. To do so I formulated a synthetic profile composed of: (1) a von
412 Kármán aperiodic component using the parameters $H = 57.3$ m (the estimated RMS height of the
413 aperiodic component, rather than the overall RMS), and k_0 and ν as derived from the best-fit model, and
414 (2) an added cosine function corresponding to amplitude 30 m and period 0.145 my. Initially this
415 created a spectral peak that was too large, so the amplitude was reduced to 24 m to match the height
416 exactly. This reiterates the point that the estimation of harmonic amplitude has significant uncertainties
417 owing to modulation by the random, aperiodic component of the spectrum. The level of uncertainty will
418 depend on the variation of the empirically pre-whitened continuous spectrum in proportion to the

419 height of the discrete spectral peak at the frequency of interest. The synthetic profile and sample
420 autocovariance are shown in Figure 8, and the resulting spectral analysis is shown in Figure 9. The
421 similarity of these plots to Figures 6 and 7, respectively, is very strong, particularly in the self-evident
422 harmonic component in the tail of the sample autocovariance (Figure 8b), and in the size spectral peaks
423 noted both on the sample power spectrum (Figure 9a) and the empirically pre-whitened spectrum
424 (Figure 9b). The only notable difference between real and synthetic is in the power at the highest
425 frequencies (Figures 7a versus 9a), which causes the real profile (Figure 6a) to have a smoother
426 appearance than the synthetic profile (Figure 8a) at the smallest scales.

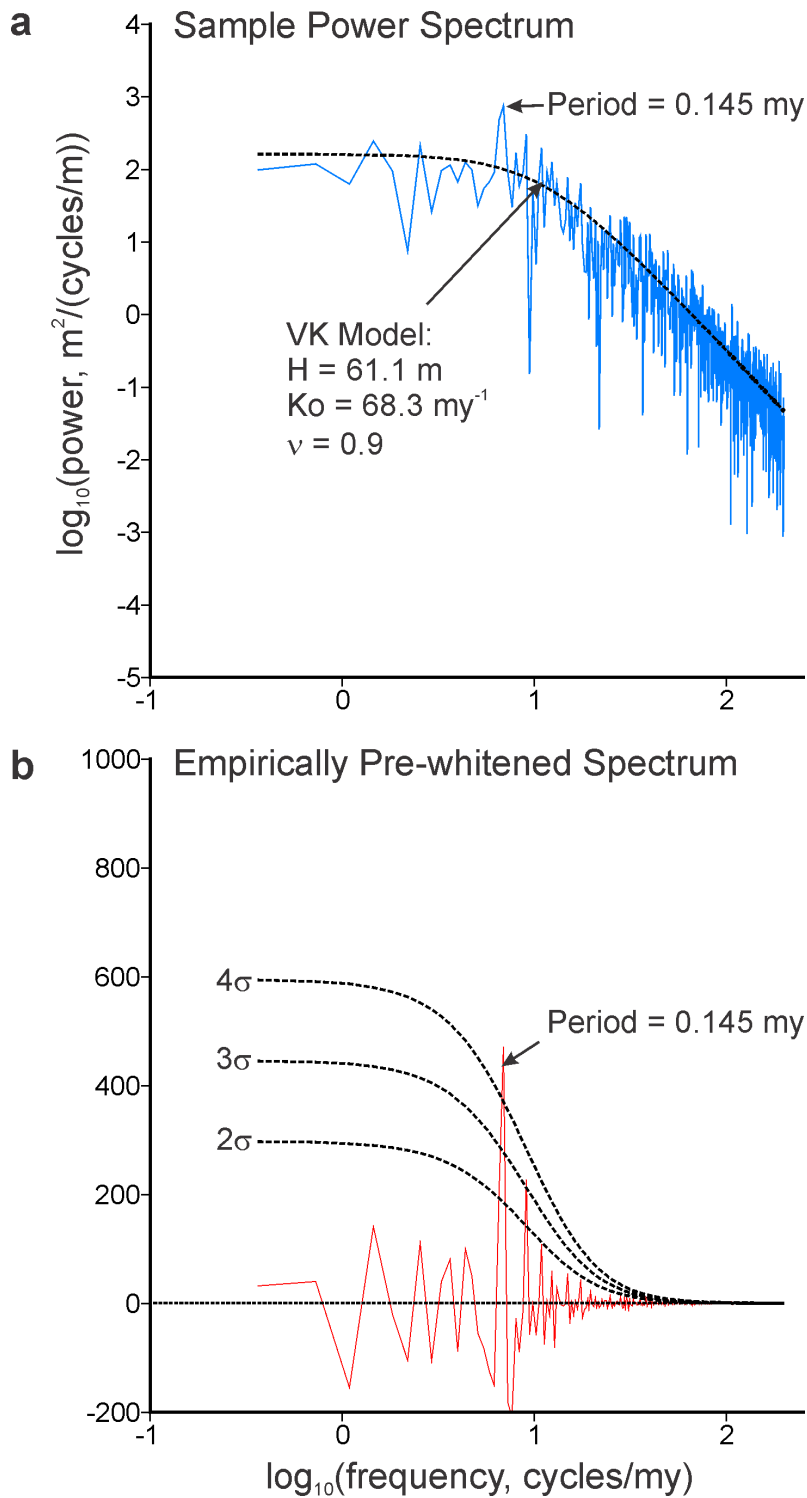
427 Spectral analysis plots for all twelve profiles are presented in the Supplementary Material. Estimated
428 von Kármán and cosine function parameters from each analysis are listed in Table 1. Periodicities were
429 detected in all but three of the profiles, and in several there were multiple periodicities detected. The
430 periods detected were highly variable, however, ranging at least an order of magnitude from 0.02 my
431 (the minimum considered for inclusion in Table 1) to 0.216 my. There is no evident clustering of values
432 at the Milankovitch periods of 0.100 my, 0.041 my or 0.026 my, although there are several detected
433 periods that are equal or close to those values. More importantly, there is no evidence of spatial or
434 temporal consistency. For example, Profiles 3, 6 and 8 are quite proximal (Figure 5), but exhibit no
435 consistency in the periods of their harmonic components (Table 1). The same inconsistency is also true
436 of Profiles 1a and 1b, and Profiles 7a and 7b (Table 1), although each pair is sited along the same flow
437 line (Figure 5) and so were generated at the same ridge crest segment but at different times.

438 To gauge the significance of each detected periodicity to variability of each profile, I calculate a
439 value R as the ratio of RMS heights of the periodic to aperiodic components, respectively. By this
440 measure (Table 1), there is a clear separation of significance between those harmonic detections with
441 periods greater than or less than the characteristic time of the best-fitting von Kármán model. Those
442 periods greater than the characteristic time, seven in all, exhibit R values ranging from 0.19 to 0.38, with

443 all but the smallest of those >0.27 . In contrast, periods less than the characteristic time exhibit R values
 444 ranging from 0.03 to 0.11, with only the largest > 0.08 . In all cases, however, the aperiodic component
 445 of the profiles is the dominant source of variability.
 446



447
 448 Figure 8. (a) Synthetic profile formed from the summation of (1) an aperiodic von Kármán profile, with
 449 parameters as noted in the text, and (2) a cosine function of amplitude 24 m and period 0.145 my. (b)
 450 Sample autocovariance (solid) computed from (a), with best-fit von Kármán model for Profile 7a
 451 (dashed). The power spectral density in Figure 9a is computed by discrete Fourier transform of the full
 452 sample autocovariance (with Hermitian symmetry), whereas the empirically pre-whitened spectrum in
 453 Figure 9b is computed in the same way after zeroing out the shaded region that fully encompasses the
 454 structural (non-zero mean) portion of the autocovariance and tapering the edges.
 455



456

457 Figure 9. (a) Sample power spectrum and (b) empirically pre-whitened spectrum calculated from the
 458 sample autocovariance of the synthetic profile shown in Figure 8. The best-fit von Kármán model is
 459 overlain on the power spectral density, and the 2 σ , 3 σ , and 4 σ upper bounds on the null hypothesis are
 460 overlain on the empirically pre-whitened spectrum. The height of the spectral peak at 0.145 my period,
 461 observed in spectral analysis of Profile 7a (Figure 7), is successfully reproduced by the synthetic profile.

462

463 **5. Conclusions and Discussion**

464 Application of an “empirical pre-whitening” spectral analysis, based on the “ $P(\lambda)$ test”
465 formulated by Priestly (1981), has enable detection of temporal periodicities at high confidence in a
466 number of profiles sampled from multibeam bathymetric data along the southern EPR. However, these
467 harmonic signals are relatively minor components of the overall variability of the profiles, which are
468 instead dominated by an aperiodic signal conforming to a continuous, rather than discrete spectrum.
469 Furthermore, the periods expressed by the harmonic signals are widely variable, and do not exhibit any
470 spatial or temporal consistency. This behavior makes the origin of harmonic signals in abyssal hill
471 morphology enigmatic, but does rule out external forcing such as may be applied by Milankovich cycle-
472 based variability in sea level. Rather, the forcing must be internal, highly localized, and subject to
473 changing conditions over time.

474 Abyssal hills generated at fast spreading rates are predominantly fault-bounded, horst-and-graben
475 structures (e.g., Macdonal et al., 1996; Macdonald, 2015). Furthermore, fault scaling parameters
476 (spacing, length, throw) are successfully modeled as random distributions constrained by scaling laws
477 (Malinverno and Cowie, 1993; Bohnenstiehl, and Carbotte, 2001). The dominant aperiodic component
478 of abyssal hills can thus reasonably be assumed to be associated with this fault-generated morphology,
479 characterized statistically by a von Kármán model defined by parameters RMS height, characteristic
480 time, and fractal dimension. The most significant harmonic contributions to abyssal hills, typically with
481 RMS heights around a quarter to a third of the aperiodic RMS, exhibit periods that are larger than the
482 characteristic time. Such variations in bathymetry could plausible be associated with variations in crustal
483 thickness associated with temporal variations in magma supply (Canales et al., 2000; Shinevar et al.,
484 2019; Parnell-Turner et al, 2020). Parnell-Turner et al. (2020), in a spectral analysis of abyssal hill
485 morphology on the flanks of the medium-spreading-rate Southeast Indian Ridge, also discerned a scale

486 of morphology (although no clear indication of periodicity) that was larger than the characteristic
487 time/width of abyssal hills. They hypothesize that variations in melt supply at <0.2 my time scales could
488 be associated either with time-varying, melt rich “porosity waves” in the mantle, or by small-scale
489 mantle heterogeneities. Investigating whether these or other mechanisms could apply to the super-fast
490 spreading southern EPR would be an important avenue of investigation for a modeling effort (though
491 beyond the scope of this paper). These results provide key observations that need to be accounted for
492 in any such effort, including the range of periods observed, their spatio-temporal variability, and their
493 topographic amplitudes.

494

495 **Acknowledgements.** The southern East Pacific Rise multibeam data used in this analysis are available
496 from the Global Multi-Resolution Topography Data Synthesis (<https://www.gmrt.org/>).

497 **References**

- 498 Babadi, B., and Brown, E.N. (2014). A review of multitaper spectral analysis. *IEEE Transactions on*
499 *Biomedical Engineering*, 61, 1555-1564.
- 500 Bhansali, R.J. (1979). A mixed spectrum analysis of lynx data. *Journal of the Royal Statistical Society*
501 *Series A*, 142, 199-209.
- 502 Bohnenstiehl, D. R., & Carbotte, S. M. (2001). Faulting patterns near 19°30'S on the East Pacific Rise: Fault
503 formation and growth at a superfast spreading center. *Geochemistry, Geophysics and Geosystems*,
504 2(9), doi: 10.1029/2001GC000156.
- 505 Canales, J. P., Collins, J. A., & Detrick, R. S. (2000). Seismic structure across the rift valley of the Mid-
506 Atlantic Ridge at 23°20' (MARK area): Implications for crustal accretion processes at slow spreading
507 ridges. *Journal of Geophysical Research*, 105, 28411–28425.
- 508 Crowley, J. W., Katz, R. F., Huybers, P., Langmuir, C. H., & Park, S.-H. (2015). Glacial cycles drive
509 variations in the production of oceanic crust. *Science*, 347, 1237-1240.
- 510 DeMets, C., Gordon, R. G., Argus, D. G., & Stein, S. (1990). Current plate motions. *Geophysical Journal*,
511 101(2), 425-478.
- 512 Durant, C., Ballu, V., Gente, P., & Dubois, J. (1996). Horst and graben structures on the flanks of the Mid-
513 Atlantic ridge in the MARK area (23°22'N): Submersible observations. *Tectonophysics*, 265, 275-297.
- 514 Garrido, J., and Garcia, J.A. (1992). Periodic signals in Spanish monthly precipitation data. *Theoretical*
515 *and Applied Climatology*, 45, 97-106.
- 516 Goff, J.A. (1995). Quantitative analysis of sea-ice draft I: Methods for stochastic modeling. *J. Geophys.*
517 *Journal of Geophysical Research*, 100, 6993-7004.
- 518 Goff, J. A., & Jordan, T. H. (1988). Stochastic Modeling of Seafloor Morphology: Inversion of Sea Beam
519 Data for Second-Order Statistics. *Journal of Geophysical Research: Solid Earth*, 93, 13589–13608.

520 Goff, J. A., & Tucholke, B.E. (1997). Multi-scale spectral analysis of bathymetry on the flank of the
521 MidAtlantic Ridge: Modification of the seafloor by mass wasting and sedimentation. *Journal of*
522 *Geophysical Research*, 102, 15,447-15,462.

523 Macdonald, K. C. (1982). Mid-ocean ridges: Fine scale tectonic, volcanic and hydrothermal processes
524 within the plate boundary zone. *Annual Reviews of Earth and Planetary Science*, 10, 155-190.

525 Macdonald, K. C. (2015). Milankovich sea level-change pumping of fault slip may enhance abyssal hill
526 growth, with spacing control by melt pumping or elastic properties. *AGU Fall Meeting*, V24A-05.

527 Malinverno, A., & Cowie. P. A. (1993). Normal faulting and the topographic roughness of mid-ocean
528 ridge flanks. *Journal of Geophysical Research*, 98, 17,921-17,939.

529 Mann, M.E., and Lees, J.M. (1996). Robust estimation of background noise and signal detection in
530 climate time series. *Climate Change*, 33, 409-445.

531 McCoy, E.J., Walden, A.T., and Percival, D.B. (1998). Multitaper spectral estimation of power law
532 process. *IEEE Transactions on Signal Processing*, 46, 655-668.

533 Müller, R. D., Seton, M., Zahirovic, S., Williams, S. E., Matthews, K. J., Wright, N. M., Shephard, G. E.,
534 Maloney, K. T., Barnett-Moore, N., Hosseinpour, M., Bower, D., J., & Cannon, J. (2016). Ocean basin
535 evolution and global-scale plate reorganization events since Pangea breakup. *Annual Reviews of*
536 *Earth and Planetary Science*, 44, 107-138.

537 Olive, J.-A., Behn, M. D., Ito, G., Buck, W. R., Escartín, J., & Howell, S. M. (2016). Response to Comment
538 on “Sensitivity of seafloor bathymetry to climate-driven fluctuations in mid-ocean ridge magma
539 supply.” *Science*, 352, 2–4.

540 Parnell-Turner, R., Sim, S.J., & Olive, J.-A. (2020). Time-dependent crustal accretion on the Southeast
541 Indian Ridge revealed by Malaysia Airlines flight MH370 search. *Geophysical Research Letters*, in
542 press, doi: 10.1029/2020GL087349.

543 Percival, D.B., & Walden, A.T. (1993). *Spectral Analysis for Physical Applications: Multi-tape and*
544 *Conventional Univariate Techniques*. Cambridge University Press, Great Britain, 583 pp.

545 Priestley, M.B. (1981). *Spectral Analysis and Time Series*. Academic Press, San Diego, California, 890 pp.

546 Scheirer, D. S., Macdonald, K. C., Forsyth, D. W., Miller, S. P., Wright, D. J., Cormier, M.-H., & Weiland, C.
547 M. (1996). A Map Series of the southern East Pacific Rise and its flanks, 15°S to 19°S. *Marine*
548 *Geophysical Research*, 18(1), 1-12.

549 Shinevar, W.J., Mark, H.F., Clerk, F., Codillo, E.A., Gong, J., Olive, J.-A., Brown, S.M., Smalls, P.T., Liao, Y.,
550 Le Roux, V., & Behn, M.D. (2019). Causes of oceanic crustal thickness oscillations along a 74-m Mid-
551 Atlantic Ridge flow line. *Geochemistry, Geophysics, Geosystems*, 20, 6123-6139.

552 Tolstoy, M. (2015). Mid-ocean ridge eruptions as a climate valve. *Geophysical Research Letters*, 42(5),
553 doi: 10.1002/2014GL063015.

554 Thomson, D.J. (1990). *Time series analysis of Holocene climate data*. *Philosophical Transactions of the*
555 *Royal Society of London Series A*, 330, 601-616.

556 Vaughn, S. (2005). A simple test for periodic signals in red noise. *Astronomy and Astrophysics*, 431, 391-
557 403.

558 von Kármán, T. (1948). Progress in the statistical theory of turbulence. *Journal of Marine Research*, 7,
559 252–264.

560

561

562 Table 1. Modeled aperiodic and detected periodic components of southern EPR profiles

563

| 564 | Profile | H, m | λ_0 , my | Period, my (min 0.02) | Z_σ (> 3.5) | α , m | R |
|-----|---------|------|------------------|--------------------------|-----------------------|--------------|------|
| 567 | 1a | 65.5 | 0.065 | 0.112 | 4.6 | 25 | 0.28 |
| 568 | | | | 0.021 | 3.9 | 3 | 0.03 |
| 569 | 1b | 83.8 | 0.089 | 0.037 | 3.9 | 7 | 0.06 |
| 570 | 2 | 74.1 | 0.050 | 0.143 | 5.3 | 35 | 0.35 |
| 571 | | | | 0.042 | 4.0 | 11 | 0.11 |
| 572 | 3 | 51.3 | 0.038 | 0.111 | 3.9 | 19 | 0.27 |
| 573 | | | | 0.082 | 6.2 | 20 | 0.29 |
| 574 | 4 | 50.4 | 0.049 | - | - | - | - |
| 575 | 5 | 50.3 | 0.043 | 0.032 | 3.7 | 6 | 0.08 |
| 576 | | | | 0.027 | 6.2 | 6 | 0.08 |
| 577 | 6 | 48.2 | 0.056 | 0.216 | 4.2 | 24 | 0.38 |
| 578 | | | | 0.022 | 4.8 | 3 | 0.05 |
| 579 | 7a | 68.3 | 0.049 | 0.145 | 5.1 | 30 | 0.33 |
| 580 | 7b | 80.3 | 0.068 | - | - | - | - |
| 581 | 8 | 41.3 | 0.034 | 0.047 | 4.1 | 11 | 0.19 |
| 582 | 9 | 58.4 | 0.065 | 0.040 | 3.7 | 7 | 0.08 |
| 583 | | | | 0.030 | 4.0 | 5 | 0.06 |
| 584 | | | | 0.025 | 7.4 | 5 | 0.06 |
| 585 | | | | 0.020 | 6.0 | 4 | 0.05 |
| 586 | 10 | 55.5 | 0.034 | - | - | - | - |

587

588 H: RMS height of best-fit von Kármán model

589 λ_0 : Characteristic time of best-fit von Kármán model

590 Z_σ : Height of spectral peak expressed as multiple of standard deviation σ .

591 α : Estimated amplitude of harmonic component.

592 R: Ratio of periodic to aperiodic RMS

593 -: No detection of harmonic component